Multishot Partial-*k*-Space EPI for High-Resolution fMRI Demonstrated in a Rat Whisker Barrel Stimulation Model at 3T

Hanbing Lu,[1] Yousef Mazaheri,[2] Rongyan Zhang,[1] Andrzej Jesmanowicz,[1] and James S. Hyde[1]*

A multishot partial-*k*-space EPI technique is presented and validated by fMRI at high spatial resolution. High-resolution phase maps corrected by phase-encoded reference scans have less off-resonance effects. Phantom studies demonstrate that this method can substantially improve partial-*k*-space EPI image formation. BOLD fMRI at submillimeter spatial resolution ($156 \times 156 \times 2000 \ \mu m^3$, $0.049 \ \mu l$) was achieved in a rat whisker barrel stimulation model using this technique. The study included eight rats, five of which were administered an intravascular contrast agent (monocrystalline iron oxide nanocolloid (MION)) after the BOLD experiments. In two rats the highest BOLD responses were in the deep layers (IV–VI), and in six rats the highest responses were on the surface and in the deep cortical layers. Most of the pixels that exhibited high BOLD responses had high blood volume weightings. The benefits of this technique are expected to increase for high-resolution fMRI at higher magnetic fields, where T_2^* is shorter. Magn Reson Med 50:1215–1222, 2003. © 2003 Wiley-Liss, Inc.

Blood oxygenation level-dependent (BOLD) contrast is commonly used in functional magnetic resonance imaging (fMRI). Theoretical analyses (1–4) and experimental data (5–9) have demonstrated that the sensitivity and specificity of the BOLD response increase as the magnetic field strength increases. However, T_2^* of brain tissues decreases as the field strength increases. For example, T_2^* of human brain gray matter is about 40 ms at 3 Tesla (8), and 25 ms at 7 T (10). This short T_2^* imposes inherent limitations on the resolution of echo-planar imaging (EPI), because of the increased point spread function (PSF) along the *y*-axis (phase-encoding direction) (11). For multishot EPI acquisitions, short T_2^* values constrain the number of *k*-space lines that can be acquired per shot. For example, for a four-shot GR-EPI using full *k*-space with a matrix size of 256×256, 166 kHz data acquisition bandwidth, and a local gradient coil with a gradient ramp time of 96 μs, the minimum echo time (TE) is about 65 ms. The TE is even longer when gradient coils with a lower slew rate, or narrower data acquisition bandwidths are used. In order to achieve a better signal-to-noise ratio (SNR), more shots must be employed, which compromises temporal resolution.

An alternative way to achieve high resolution in fMRI is to employ half-*k*-space data acquisition. Half-*k*-space EPI allows data to be acquired in less time than that required by full-*k*-space EPI by a factor of ~1/2 for any desired matrix, and the TE is shorter because the central *k*-space lines are collected first. In fMRI, short data acquisition times and TEs are desirable because they enable high spatial/temporal resolution imaging without compromising the SNR (12). Additionally, short data acquisition times can reduce the image distortions that are typically found in EPI, and shorter TEs reduce signal dropout in regions with strong susceptibilities.

Another benefit of half-*k*-space data acquisition is the narrower PSF, which is critically important in high-resolution fMRI. Jesmanowicz et al. (13) demonstrated that the *y*-axis PSF arising from T_2^* decay in full-*k*-space acquisition is $3^{1/2}$ times wider than that in a single-shot half-*k*-space acquisition. It can be shown that the *y*-axis PSF (12–14) in two-shot half-*k*-space acquisition is narrower by a factor of 2 than that in single-shot half-*k*-space acquisition. Blurring and loss of signal intensity occur when the width of the PSF is similar to or greater than the voxel dimension in the *y*-direction. As a result, isolated activated voxels or regions that are one voxel wide in the phase-encoding direction are more difficult to detect with single-shot EPI than with multishot EPI. These effects can be expected to be more pronounced at high field strength, in anatomical regions where T_2^* is short, and at high spatial resolution.

A phase map is required for image formation using half-*k*-space acquisition, and a higher-resolution phase map is preferable (15,16). In EPI-based techniques, the resolution of the phase map in the phase-encoding direction is limited by the number of overscan lines due to T_2^* constraints. However, if a multishot *k*-space data acquisition scheme (17–20) is employed, the total number of overscan lines can be effectively increased, resulting in a high-resolution phase map. To account for physiological motion and system instability, navigator echoes (21,22) are typically acquired to correct intersegment variations.

Off-resonance effects result in geometric distortions and intensity deviations in EPI acquisitions due to long data acquisition times, which have confounding effects on phase maps and result in complex artifacts in half-*k*-space images. Non-phase-encoded reference scan techniques, which apply either nonlinear (23) or linear (24,25) phase

[1]Department of Biophysics, Medical College of Wisconsin, Milwaukee, Wisconsin.

[2]Department of Radiology, University of California–San Diego, San Diego, California.

*Correspondence to: Professor J.S. Hyde, Biophysics Research Institute, Medical College of Wisconsin, 8701 Watertown Plank Rd., Milwaukee, WI 53226. E-mail: jshyde@mcw.edu

corrections to the image space data, can substantially reduce ghosting artifacts in EPI. However, when B_0 inhomogeneity is relatively high, these techniques become inadequate. In this case, a phase-encoded reference scan employing nonlinear phase corrections (26) would be a preferable approach for half-k-space phase corrections.

In this work, we describe an approach for high-resolution fMRI at high field strength that combines the benefits of a half-k-space acquisition with interleaving, and employs phase-encoded reference scans with navigator echoes for phase corrections. In particular, we used a multishot half-k-space acquisition to improve the SNR and PSF, and created higher-resolution phase maps with minimal compromise in temporal resolution. Nonlinear phase correction with phase-encoded reference scans was used to reduce off-resonance effects and ghosting artifacts. Navigator echoes were used to correct for intersegment phase variations due to physiological motion and system instability. Strong crusher gradients were applied to suppress B_0-fluctuation-induced temporal variations in EPI image scans from the disturbance of the steady-state free precession (SSFP) (27). A sliding-window data acquisition scheme was employed to decrease intersegment phase and magnitude modulations (17). Phantom studies demonstrated that this technique can significantly improve half-k-space image formation. BOLD fMRI in a rat model at submillimeter spatial resolution, with a temporal resolution of 2 s, was achieved using this method. A preliminary report of this work was previously published in an abstract (28).

MATERIALS AND METHODS

Imaging Methods

For a single-shot, gradient-recalled, blipped EPI sequence, ignoring T_2^* decay, the MR signal can be modeled as:

$$S(k_x, q\Delta k_y) = \iint M(x', y')\exp\{-i[k_x + (-1)^q\varepsilon]x' - ik_y y'\}$$
$$\times \exp\{-i\lambda(x', y')t(k_x, k_y)\}\, dx'\, dy',\quad [1]$$

where $M(x', y')$ is the object to be imaged, $\lambda(x', y')$ is the spatially-dependent magnetic field inhomogeneity, and $t(k_x, k_y)$ is the temporal offset measured from the center of the RF excitation pulse to the acquisition of the (k_x, k_y) point, given by:

$$t(k_x, k_y) = \text{TE} + (-1)^q k_x/b + k_y/c.\quad [2]$$

Here TE is the echo time, q is the phase-encoding step, $k_x = n\Delta k_x$, $k_y = q\Delta k_y$, $\Delta k_x = 2\pi/FOV_x$, and $\Delta k_y = 2\pi/FOV_y$. FOV_x and FOV_y are the fields of view in the readout and phase-encoding directions, respectively. The parameters b and c are the k-space traverse rates along k_x and k_y, respectively. These rates are related to the scan settings, including the data acquisition bandwidth and the FOV. ε is the k_x inconsistency between the forward and backward scan lines arising from group delay of the anti-alias filter, as well as the variations of the rising and falling edges of the readout gradient. For simplicity, a constant ε is assumed in

this analysis. An inverse Fourier transform of Eq. [1] along k_x results in:

$$I(x, q\Delta k_y) = \iint M(x', y')\exp\{-i[(-1)^q\varepsilon x' + \lambda(x', y')TE]\}$$
$$\times \exp\{-ik_y[y' + c^{-1}\lambda(x', y')]\}$$
$$\times \int \exp\{ik_x[x - x' - (-1)^q b^{-1}\lambda(x', y')]\}\, dk_x dx'\, dy',\quad [3]$$

where $\int \exp\{ik_x[x - x' - (-1)^q b^{-1}\lambda(x', y')]\}\, dk_x = \delta(x - x' - (-1)^q b^{-1}\lambda(x', y'))$. The pixel shift along k_x is typically small compared to the pixel size and therefore can be ignored.

The field inhomogeneity $\lambda(x', y')$ and variations of ε along k_x can result in additional ghosting artifacts and spatially-varying image intensity changes. From Eq. [3], it follows that the phase accumulation due to $\lambda(x', y')$ is proportional to k_y and TE. EPI phase correction methods based on non-phase-encoded reference scans, such as a full separate reference scan (23) or two reference scan lines (24,25), ignore the phase term $\exp[-ik_y \cdot c^{-1}\lambda(x', y')]$ in Eq. [3]. This term can have confounding effects on the phase map formation when $\lambda(x', y')$ is large. A reference scan with the same amount of phase encoding can be applied to reduce these effects (26). Consequently, when half-k-space data acquisition is used, a phase map based on a phase-encoded reference scan has less off-resonance effects.

The pulse sequence employing the phase-encoded reference scan scheme is shown in Fig. 1. The phase-encoding blips in the reference scan have the same amplitude as in the image scan. The first blip in the reference scan was skipped. In addition, the timing of the EPI data acquisition in the image scan was shifted by one cycle (T_{cyc}) away from the excitation pulse (see Fig. 1). As a result, the even k-space lines in the image scan, and the odd k-space lines in the reference scan have the same amount of phase-encoding but traverse in opposite directions. A 15-ms crusher gradient with 80% of the full gradient strength was applied in each segment to suppress B_0-fluctuation-induced temporal signal variations due to the disturbance of the SSFP. Sliding data acquisition windows between segments were also implemented. In a multishot case (m shots), m reference scans were acquired, followed by image scans, with the prephase and TE shift changed for each shot. Specifically, from shot to shot, the TE shift was progressively increased by a factor of T_{cyc}/m, and the prephase for the nth shot was calculated using the formula:

$$\text{prephase} = (\text{overscan} \times m - n + 1) \times \Delta k_y,\quad [4]$$

where Δk_y is the phase-encoding step in full-k-space imaging.

Images were reconstructed in three steps:

1) Even and odd lines were reordered. Navigator-echo correction for each segment was calculated in image space as well as in k-space. This was carried out in two steps:

a) A constant phase factor was derived in image space. The navigator echoes were Fourier-transformed into image

FIG. 1. Pulse sequence diagram for half-*k*-space gradient-echo EPI with a phase-encoded reference scan. A navigator echo is acquired at the beginning and a strong crusher gradient is applied at the end of each shot. The first blip in the reference scan is skipped. Overscan lines are acquired in each shot so that every image has a separate phase map. For the multishot case (*m* shots), reference scans are repeated *m* times followed by image scans, with the prephase pulse and TE shift changed correspondingly.
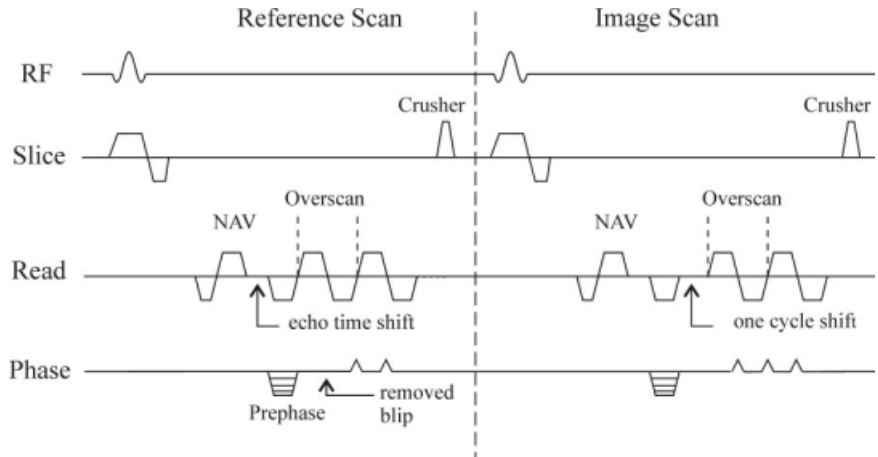
space and the navigator echo from the first shot was chosen as the reference. For the *n*th shot, a constant phase factor φ_n was calculated using a magnitude-weighted phase average from all data points. This phase factor was compared with that of the reference navigator (φ_{ref}). A constant phase difference for the *n*th shot μ_n was derived using the formula: $\mu_n = \varphi_{ref} - \varphi_n$.

b) The displacement *d* for each shot was derived in *k*-space. Following the Fourier shift theorem, a global displacement *d* in image space induces a linear phase ramp in *k*-space. The phase of the *n*th navigator echo was fitted to $\Delta\varphi[k] = 2\pi kd/N + \mu_n$ using a *k*-space signal magnitude-weighted, least-squares approach (29). The phase of the navigator echo was median-filtered and unwrapped before linear fitting.

2) EPI phase correction was performed. The phases of the image scans were corrected using the reference scans. Specifically, the reference scan data and image scan data were Fourier-transformed along the readout direction. The phases of the even lines of the reference scans were calculated on a point-by-point basis. The same calculations were done for the odd lines of the image scan that had the same amount of phase-encoding but traversed in the opposite *k*-space direction. Phase correction is performed as follows: let the phase of the *i*th point at the *2j*th line of the reference scan be $e^{i\theta_{2j}[i]}$ and the phase of the *i*th point at the (*2j+1*)th line in the image scan be $e^{i\varphi_{2j+1}[i]}$. The phase in the (*2j+1*)th line of the image scan is set to the new value $e^{i\psi_{2j+1}[i]}$ using the formula:

$$e^{i\psi_{2j+1}[i]} = e^{-i\theta_{2j}[i]} \cdot e^{i\varphi_{2j+1}[i]}. \qquad [5]$$

A threshold of 5% of the averaged amplitude of the projection data was chosen. The phase correction factor was set to 1 (no correction) for any data point with amplitude less than the threshold. After this correction, the even and odd lines in the image data have the same amount of *k*-space shift resulting from gradient timing, eddy currents, the frequency response asymmetry of the analog filter, etc. Instead of using the same set of phase correction factors for all image scans, as in Ref. 26, we calculated the phase factors for each image separately.

3) Half-*k*-space phase correction was performed. The overscan lines from each shot and an equal number of

low-frequency lines from the other side of *k*-space were combined, zero-padded, and Fourier-transformed to form a phase image. The phase image had low resolution in the phase-encoding direction. The original *k*-space data were Fourier-transformed, phase-corrected using the low-resolution phase map, inverse Fourier-transformed to *k*-space, and Hermitian-conjugated and Fourier-transformed to generate the final image. By interleaving, effectively more overscan lines were used for the phase map formation. For example, for a two-shot half-*k*-space EPI with matrix size of 128 × 128, 16 overscan lines were acquired in each shot. A 128 × 64 resolution phase map can be generated, which was found to improve image quality significantly.

Spin-echo, gradient-recalled, and simultaneous spin-echo/gradient-recalled half-*k*-space EPI sequences employing the described correction scheme were implemented on a 3 T BIOSPEC 30/60 scanner (Bruker Medizintechnik GMBH, Karlsruhe, Germany).

Phantom Study

A grid phantom was used to study the effects of different correction schemes and the number of overscan lines on partial-*k*-space image formation. The phantom was 16 cm in diameter, with a T_2^* value of about 50 ms. Some small air bubbles were left inside the phantom to simulate magnetic field inhomogeneities. A poorly-shimmed slice was chosen for this study. The experiment was carried out using a local gradient coil and an RF coil (30). A comparison between linear (two internal reference scan lines) and nonlinear (phase-encoded reference scan) phase corrections was made. The scan parameters were FOV = 19.2 cm, data acquisition bandwidth = 166 kHz, slice thickness = 1.5 mm, and matrix = 128 × 128. The number of overscan lines was systematically changed from 8 to 16 to 32, with TE values of 14, 20.3, and 38.9 ms, respectively.

High-Resolution fMRI Using a Rat Whisker Barrel Stimulation Model

This method was applied to BOLD fMRI at a spatial resolution of 156 × 156 × 2000 μm^3 in a rat whisker barrel stimulation model. The animal protocols were approved

by the Laboratory Animal Safety Committee of the Medical College of Wisconsin.

Animal Preparations

The animal preparation protocol was adapted from Refs. 31 and 32. Eight male Sprague-Dawley rats weighing 250–350 g were anesthetized with 1–2% (v/v) isoflurane (isoflurane vaporizer, model 100F; Ohio Medical Products, Madison, WI) in a (1:1) mixture of O_2:air during surgery. The right femoral artery was cannulated for blood pressure monitoring and blood gas measurements. The right femoral vein was cannulated for drug and saline delivery. A Harvard rodent ventilator (model 683; Harvard Apparatus, South Natick, MA) was used for artificial ventilation. The tidal volume and frequency of the ventilator were adjusted to keep blood gases within the normal range. The arterial blood pressure was continuously monitored. Rectal temperature was maintained at 37°C ± 0.5°C by a temperature-controlled water-heating pad. The heads of the rats were fixed with an in-house-made bite bar and ear bar to minimize motion artifacts during the fMRI experiments. A neuromuscular blocking agent (Gallamine, 250 mg/kg i.v.) was used during the fMRI experiment to further minimize motion artifacts. After surgery, the anesthesia was switched from isoflurane to 5% α-chloralose in propylene glycol, with an initial dose of 50 mg/kg followed by 40 mg/kg/hr.

Experimental setup

Gradient coil. A 12.5-cm I.D., water-cooled, torque-balanced, three-axis local gradient coil designed by Lu et al. (33) was used in this study. This coil has an efficiency of $2.13 \, \text{mT} \cdot \text{m}^{-1} \cdot \text{A}^{-1}$ along *x*, $2.08 \, \text{mT} \cdot \text{m}^{-1} \cdot \text{A}^{-1}$ along *y*, and $4.12 \, \text{mT} \cdot \text{m}^{-1} \cdot \text{A}^{-1}$ along *z*, and was driven at 96 μs rise time.

RF coils. A saddle coil of 9-cm I.D. and 10-cm length was used for RF transmitting, and a 1.5-cm I.D. surface coil was used for signal reception. The receive coil had a free space unloaded Q value of 380. The isolation between the transmit and receive coils was about 35 dB under loaded conditions.

Whisker stimulator. An in-house-made whisker stimulator was used in this study (34). A stimulus waveform of the desired frequency and duration was generated by a laptop computer, power-amplified, and used to drive a piezoelectric device. A small comb (1.5 cm long, 0.8 cm high, 12 struts) was connected to the piezoelectric device through an actuator arm (0.75 m long). The backward/forward movement of the comb was about 2.5 mm. The distance between the rat face and the comb was about 1 cm. Before the rat was put into the magnet, the whiskers on the left side were cut completely and the whiskers on the right side were cut to a length of about 3 cm, so that only the long whiskers on the right side were stimulated. No artifacts induced by the whisker stimulator were observed in this study.

Scan Method

Slice localization to the whisker barrel cortex was determined as follows: Medial sagittal anatomical images were scanned using a fast low-angle shot (FLASH)-type sequence with TR = 500 ms, TE = 18 ms, and FOV = 3.5 cm. The interface between the hard and soft palates was chosen as the reference, which corresponds approximately to interaural 11.2 mm according to the stereotaxic coordinates of the rat brain. A 2-mm-thick coronal slice with its center at 4.6 mm caudal to the reference covered the whisker barrel region (35).

The stimulus paradigm was a block design consisting of four cycles of 64 s off and 32 s on. The scan sequence was a two-shot partial-*k*-space EPI with 16 overscan lines in each shot. The scan parameters were FOV = 2 cm, matrix = 128 × 128, TE = 24 ms, slice thickness = 2.0 mm, effective TR = 2 s (1 s per shot), and in-plane resolution = 156 × 156 μm² (voxel volume = 0.049 μl). The experiment was repeated three times and images were averaged to improve the SNR. Low-resolution fMRI data were acquired from each rat before the high-resolution experiment was conducted. The scan parameters for the low-resolution fMRI experiment were single-shot full-*k*-space EPI, FOV = 3.5 cm, matrix = 64 × 64, slice thickness = 2.0 mm, and in-plane resolution = 547 × 547 μm² (voxel volume = 0.6 μl). Anatomical images were acquired using the same sequence and with the same parameters as in the BOLD experiment so that misregistration between the anatomical and functional images was minimal. To enhance the contrast of the anatomical images, five rats were administered an intravascular paramagnetic contrast agent (monocrystalline iron oxide nanocolloid (MION)) with the iron dose of 12 mg/kg (36).

RESULTS

Phantom Study

Figure 2 shows the phantom images acquired using different phase correction methods with different numbers of overscan lines. Column a shows the images acquired using single-shot gradient-recalled EPI (SS-GR-EPI) with linear phase correction (two internal reference scan lines). Column b shows the images acquired with SS-GR-EPI using phase-encoded reference scans. Column c shows the images acquired using a two-shot (TS) GR-EPI sequence with the phase corrected by phase-encoded reference scans. All images were acquired under the same shimming conditions with the same data acquisition bandwidths.

A comparison of the images in columns a and b of Fig. 2 for partial-*k*-space EPI using SS-GR-EPI shows that as the number of overscan lines increases from 8 to 32, the image intensity around strong susceptibility regions is more homogeneous and distortion is decreased, demonstrating the benefits of high-resolution phase maps. Images Ia–c (eight overscan lines) appear to have less susceptibility artifacts, and are more blurred than the other images. This is due to the low-pass filter of the low-resolution phase maps. The arrows in IIa and IIb indicate that images reconstructed using phase-encoded reference scans have reduced artifacts. Ghosting artifacts are more severe in images with eight (Ia and Ib) or 32 overscan lines (IIIa and IIIb) than in images with 16 overscan lines (IIa and IIb). However, these ghosting artifacts are caused by different factors. The ghosting artifacts in images Ia and Ib are due to insufficient overscan lines (low-resolution phase maps), while the

FIG. 2. Comparison of ghosting artifacts and susceptibility effects in partial-*k*-space image formation. Column **a** and **b:** SS-EPI images with phase corrected by internal reference and phase-encoded reference scans, respectively. Column **c:** TS-EPI images with phase corrected by phase-encoded reference scans. The images in the first row used eight overscan lines; images are blurred due to the low-pass filter of the low-resolution phase maps. The second row used 16 overscan lines. IIb has less susceptibility-induced artifacts than IIa, as indicated by the arrows. Ghosting artifacts are also slightly decreased. The same observations can be made in IIIa and IIIb, which used 32 overscan lines. Interleaving (the third column) further improved image quality. Scan parameters: FOV = 19.2 cm, matrix = 128 × 128, FOV = 19.2 cm, data acquisition bandwidth = 166 kHz, slice thickness = 1.5 mm.
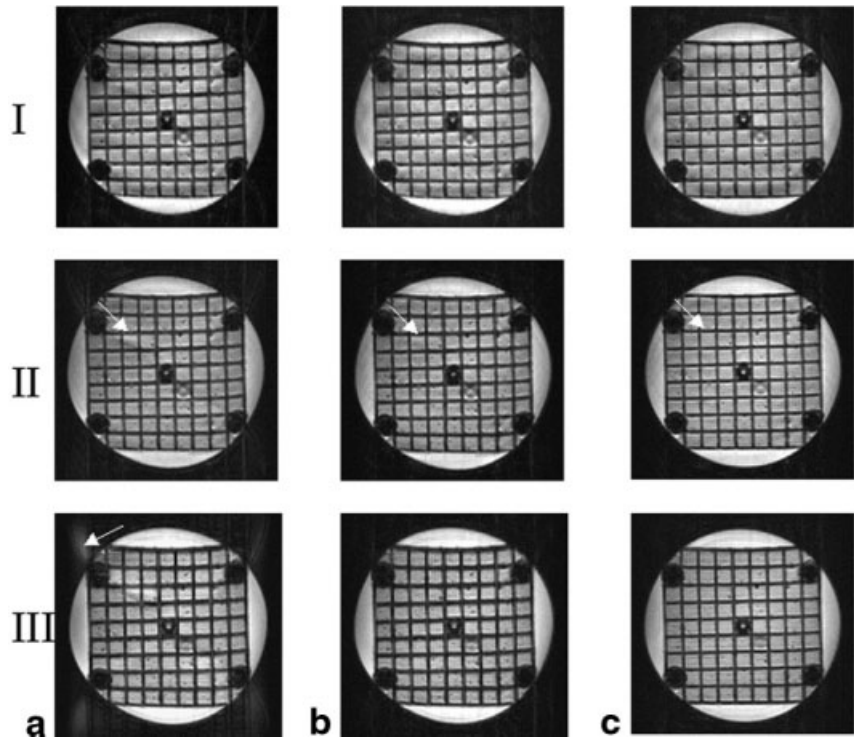
ghosting artifacts in images IIIa and IIIb are due to low SNR (minimum TE = 38.9 ms). These data indicate that even though a higher-resolution phase map is preferable, 16 overscan lines are practical for SS-GR-EPI because as the number of overscan lines increases, TE increases and SNR decreases.

A comparison of columns b and c of Fig. 2 shows that images acquired with TS-GR-EPI (column c) have more homogenous intensities and reduced ghosting artifacts. The distortions around strong susceptibility regions are still visible, but are much smaller than in column b, demonstrating the benefits of interleaving. It is worth noting that image intensity in IIIc (16 overscan lines in each shot) is more homogenous than in IIc (eight overscan lines for each shot), and that the distortions around strong susceptibility regions are smaller. Images acquired using TS-GR-EPI with 32 overscan lines had the best quality in this study.

These data demonstrate that distortions and susceptibility artifacts in half-*k*-space images are reduced by nonlinear phase corrections with phase-encoded reference scans, and are further improved by *k*-space interleaving.

Time-Course Stability

Noise sources in fMRI time series include contributions from intrinsic thermal noise in each individual image as well as inter-image variations resulting from physiological fluctuations, cardiac and respiratory motion, and system instabilities. The latter contributions are serious concerns in EPI with interleaving, since data are acquired at different TRs for image formation. Part of the validation that allows the sequence presented here to be applicable to fMRI is to compare time-course noise fluctuations of this method with standard EPI at the same resolution. When the

resolution is at a cortical laminar thickness level (<200 μm), image SNR is much poorer in SS-EPI than in multishot EPI, which could compromise the comparison. We compared time-course stabilities at an in-plane resolution of 537 × 537 μm^2 (FOV = 3.5 × 3.5 cm, matrix = 64 × 64). Due to the sensitivity profile of the surface coil, image SNR in the barrel cortex regions is 170–200 for single- and multishot EPI (regions 1 and 2 of Fig. 3a), while it is 90–100 in the thalamus (region 3 of Fig. 3a). SNR is calculated by the difference between signal and background noise divided by background noise, and background noise is the averaged signal intensity from 40 pixels that are out of the brain region and free of ghosting. The low SNR in the thalamus region is used to simulate time-course stabilities at high resolution. In addition, when multishot EPI is used to acquire data at this resolution, it is more sensible
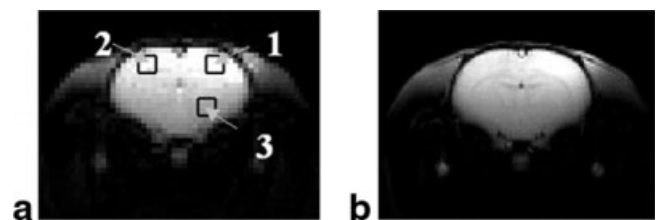

FIG. 3. **a:** Image acquired using four-shot EPI with a resolution of 537 × 537 × 2000 μm^3. Boxes 1 and 2 indicate pixels in the whisker barrel cortex regions of both hemispheres that have an SNR of 170–200, and box 3 shows pixels in the thalamus region with an SNR of 90–100. Each box contains nine pixels. The signal SD variation over the mean is averaged to quantify time-course variability. **b:** A reference image acquired using a FLASH sequence with a resolution of 137 × 137 × 2000 μm^3. No obvious artifacts were observed in the EPI image.

Table 1
Comparison of Time Course SD Over Mean From Regions 1, 2, and 3 of Fig. 3

	Regular EPI (1-shot)	Phase-encoded (1-shot)	Phase-encoded (2-shot)	Phase-encoded (4-shot)
Region 1	0.88 ± 0.17%	0.89 ± 0.15%	0.73 ± 0.11%	0.78 ± 0.06%
Region 2	0.89 ± 0.17%	0.87 ± 0.18%	0.76 ± 0.18%	0.77 ± 0.18%
Region 3	1.29 ± 0.5%	1.32 ± 0.36%	1.28 ± 0.45%	1.02 ± 0.35%

to use full k-space rather than half k-space. As such, all data for the comparison of time-course stabilities were acquired using full-k-space EPI. Figure 3b is a reference image acquired using a FLASH sequence with a resolution of $137 \times 137 \times 2000$ μm³. No obvious artifacts were observed in the EPI image (Fig. 3a). TE was kept at 29 ms, and the effective TR was kept at 2 s for one and two shots, and 4 s for four shots (1 s per shot) to minimize alterations in the inflow characteristics. The number of repetitions was changed so that 100 image frames were acquired in each experiment. The signal standard deviation (SD) over the mean was used to quantify time course variability. The results from three rats are summarized in Table 1. These data demonstrate that this method and regular EPI have comparable time-course fluctuations when SS-EPI is used (when imaging anesthetized rats), and signal fluctuations in regions of lower SNR are reduced for multishot EPI.

fMRI Study

A robust BOLD response was consistently detected in all eight rats. However, with some of the rats it took about 1.5 hr for the BOLD response to stabilize, which is similar to findings in a rat forepaw stimulation model reported by Ogawa et al. (37). Functional data analyses were carried out using the AFNI software package (38). Activation maps were generated using the cross-correlation method (39). Figure 4a shows a BOLD activation map ($p < 0.005$) superimposed on the first EPI anatomical image. Figure 4b is an enlarged view of the activation map in Fig. 4a. Figure 4c is the same activation map superimposed on an anatomical image with contrast enhanced by MION. Figure 4d is the postcontrast anatomical image without the activation

map superimposed. Figures 4e and f are rCBV maps with and without activation map superimposition, respectively. The rCBV map was calculated as follows: let S_{pre} and S_{post} represent pre- and postcontrast signal intensities, respectively, and assuming that pre- and postcontrast data are acquired at the same TE, pixel-wise rCBV can be calculated using $\ln(S_{pre}/S_{past})$/TE (36). Figure 5 shows the averaged time courses from 20 pixels centered at the arrow in Fig. 4b. The percent signal changes varied from 1.6% to 6.5%. The averaged percent signal change from eight rats was about 2.3% at this spatial resolution ($156 \times 156 \times 2000$ μm³, 0.049 μl voxel volume), while it was about 1.1% at a resolution of $547 \times 547 \times 2000$ μm³, (0.6 μl voxel volume).

Pixels with high BOLD responses are located in both the surface layers and the deep layers. The arrow in Fig. 4b indicates 16 pixels with high BOLD response (yellow pixels) that appear to be radial to the cortical surface. These yellow pixels all have low signal intensities (dark spots) in the postcontrast image (4d) and high rCBV values (bright) in the rCBV map (4f), indicating relatively high blood volume weightings in these pixels.

Of the eight rats scanned using the GR-EPI sequence, two had the highest BOLD response in the deep layers (IV–VI), and six had the highest BOLD response on the surface and in the deep layers.

DISCUSSION

In high-resolution fMRI using EPI-based sequences, high SNR, narrow PSF, minimal distortions, and reasonable temporal resolution are critical. The technique presented
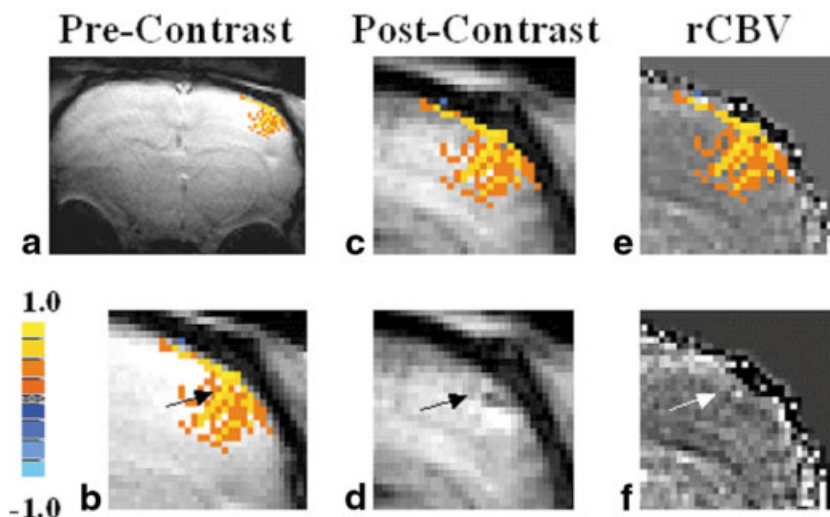

FIG. 4. Cross-correlation activation maps superimposed on different anatomical images. The first column shows BOLD activation maps superimposed on the first EPI anatomical image. **b:** An enlarged view of the activation map in **a**. The second column shows MION-enhanced anatomical images with and without superimposition of the activation map, respectively. The third column shows rCBV maps with and without superimposition of the activation map, respectively. The arrow in **b** indicates pixels with high BOLD response (yellow pixels) that appear to be radial to the cortical surface. These pixels have low signal intensities in the postcontrast (**d**) and high rCBV weighting image (**f**).
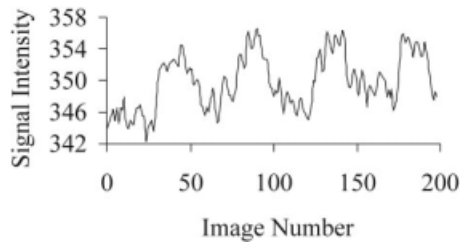
FIG. 5. Time courses averaged from 20 pixels centered at the arrow in Fig. 4b.

here combines the benefits of half-*k*-space acquisition, interleaving, and a phase-encoded reference scan scheme for phase corrections, significantly improving half-*k*-space image formation. By using two-shot half-*k*-space EPI with three averages, we were able to detect a robust fMRI response with a TE of 24 ms and a matrix size of 128 × 128 (voxel volume = 0.049 µl) at a temporal resolution of 2 s.

Susceptibility gradients are linearly proportional to field strength, and T_2^* decreases as field strength increases. As a result, T_2^* blurring and susceptibility artifacts are more severe at high fields, which necessitates a narrower data acquisition window. The partial-*k*-space technique starts data acquisition at TE close to zero, which takes advantage of the high signal intensity at high field strength before the signal decays away. Phase-encoded reference scans can reduce susceptibility artifacts, which are further improved by *k*-space interleaving. Although the sequence was implemented at 3 T, it can be readily extended to ultra-high fields to achieve high temporal and spatial resolution in a straightforward way.

The properties of motion-induced ghosting artifacts and signal variation in fMRI time courses are different in EPI phase corrections using internal reference scans compared to those using separate reference scans. Small motions do not result in ghosting artifacts in SS-EPI using internal reference scans, because the data acquisition window is typically <80 ms in SS-EPI, and the reference data are acquired within the data acquisition window. As a result, the reference data are dynamically adapted to motion. However, motion still causes image displacement and increased signal variations in EPI time courses. In phase corrections using separate reference scans, the reference data are typically acquired at the beginning or the end of the time series. Phase errors due to motion and system instability during the experiment cannot be corrected by reference data, and result in ghosting artifacts and increased variations in fMRI time courses. This problem can become pronounced in multishot EPI because data are acquired during different TRs. In fMRI of anesthetized rats, subject motion is not a major issue, and multishot EPI using phase-encoded reference scans does not result in increased variations in EPI time courses, as shown in Table 1. Note that the time-course variations in regions 1 and 2 of Fig. 3 (SNR = 170−200) are very similar in all of the methods, which indicates that time-course noise in these regions is dominated by physiological fluctuations.

To avoid compromising the SNR, we used a slice thickness of 2 mm, which covered most of the barrel columns of five rows, since each barrel has a diameter of about 350−400 µm (40). Although the in-plane resolution was 156 × 156 µm², which approximately matches the thickness of the cortical layers, overlapping of the activations between cortical layers can be expected because of the arc-shaped organization of the barrel columns (40). Nevertheless, the BOLD response we observed was not uniform across cortical layers. Our data show that the pixels with high BOLD responses were located on the surface and in the deep cortical layers, and that most of these pixels were in the dark spots of the anatomical image after MION administration, indicating relatively high blood volume (see Figs. 4b and d). These data support previous theoretical simulations (2−4,41). Further work is needed to quantify the relationship between the BOLD response and the cerebral blood volume (CBV).

The localization and functional specificity of the BOLD response using gradient-echo sequences remain unclear, particularly at high spatial resolution at high field. Logothetis et al. (42) reported highly layer-specific BOLD responses in the monkey visual cortex, while Harel et al. (43) observed a nonspecific BOLD response in the cat visual cortex. However, our data show that the high BOLD responses were located on the surface and in the deep cortical layers. These discrepancies may be due to the differences in animal models and field strengths used in these studies.

In conclusion, multishot half-*k*-space EPI enables the detection of functional activation at a submillimeter resolution at 3 T, with a temporal resolution of 2 s. The benefits of this technique are expected to increase for high-resolution fMRI at higher magnetic fields.

ACKNOWLEDGMENTS

REFERENCES

1. Ogawa S, Menon RS, Tank DW, Kim S-G, Merkle H, Ellermann JM, Ugurbil K. Functional brain mapping by blood oxygenation level-dependent contrast magnetic resonance imaging. Biophys J 1993;64:800−812.
2. Boxerman JL, Bandettini PA, Kwong KK, Baker JR, Davis TJ, Rosen BR, Weisskoff RM. The intravascular contribution to fMRI signal changes: Monte Carlo modeling and diffusion-weighted studies in vivo. Magn Reson Med 1995;34:4−10.
3. Kennan RP, Zhong J, Gore JC. Intravascular susceptibility contrast mechanisms in tissues. Magn Reson Med 1994;31:9−21.
4. Fujita N. Extravascular contribution of blood oxygenation level-dependent signal changes: a numerical analysis based on a vascular network model. Magn Reson Med 2001;46:723−734.
5. Turner R, Jezzard P, Wen H, Kwong KK, Le Bihan D, Zeffiro T, Balaban RS. Functional mapping of human visual cortex at 4 and 1.5 tesla using deoxygenation contrast EPI. Magn Reson Med 1993;29:277−279.
6. Gati JS, Menon RS, Ugurbil K, Rutt BK. Experimental determination of the BOLD field strength dependence in vessels and tissue. Magn Reson Med 1997;38:296−302.
7. Lee SP, Silva AC, Ugurbil K, Kim SG. Diffusion-weighted spin-echo fMRI at 9.4 T: microvascular/tissue contribution to BOLD signal changes. Magn Reson Med 1999;42:919−928.

8. Bandettini PA, Wong EC, Jesmanowicz A, Prost R, Cox RW, Hinks RS, Hyde JS. MRI of human brain activation at 0.5 T, 1.5 T, and 3.0 T: comparison of ΔR_2^* and functional contrast to noise ratio. In: Proceedings of the 2nd Annual Meeting of ISMRM, San Francisco, 1994. p 434.

9. Bandettini PA. Magnetic resonance imaging of human brain activation using endogenous susceptibility contrast. Ph.D. dissertation, Medical College of Wisconsin, Milwaukee, WI, 1995.

10. Yacoub E, Shmuel A, Pfeuffer J, Moortele PF, Adriany G, Andersen P, Vaughan JT, Merkle H, Ugurbil K, Hu X. Imaging brain function in humans at 7 Tesla. Magn Reson Med 2001;45:588–594.

11. Farzaneh F, Riederer SJ, Pelc NJ. Analysis of T_2 limitations and off-resonance effects on spatial resolution and artifacts in echo-planar imaging. Magn Reson Med 1990;14:123–139.

12. Hyde JS, Biswal BB, Jesmanowicz A. High-resolution fMRI using multislice partial k-space GR-EPI with cubic voxels. Magn Reson Med 2001;46:114–125.

13. Jesmanowicz A, Bandettini PA, Hyde JS. Single-shot half k-space high-resolution gradient-recalled EPI for fMRI at 3 Tesla. Magn Reson Med 1998;40:754–762.

14. Haacke EM, Brown RW, Thompson MR, Venkatesan R. Magnetic resonance imaging: physical principles and sequence design. New York: John Wiley & Sons, Inc.; 1999.

15. Margosian P, Schmitt F, Purdy D. Faster MR imaging with half the data. Health Care Instrum 1986;1:195–197.

16. Purdy DE. A Fourier transform method of obtaining high resolution phase map for half-Fourier imaging. In: Proceedings of the 7th Annual Meeting of SMRM, San Francisco, 1988. p 968.

17. McKinnon GC. Ultrafast interleaved gradient-echo-planar imaging on a standard scanner. Magn Reson Med 1993;30:609–616.

18. Butts K, Riederer SJ, Ehman RL, Thompson RM, Jack CR. Interleaved echo planar imaging on a standard MRI system. Magn Reson Med 1994;31:67–72.

19. Tan SG, Song AW, Wong EC, Hyde JS, Li SJ. High resolution fMRI with interleaved EPI. In: Proceedings of the 3rd Annual Meeting of ISMRM, Nice, France, 1995. p 796.

20. Kim SG, Hu X, Adriany G, Uǧurbil K. Fast interleaved echo-planar imaging with navigator: high resolution anatomical and functional image at 4 Tesla. Magn Reson Med 1996;35:895–902.

21. Hu X, Kim S-G. Reduction of signal fluctuation in functional MRI using navigator echoes. Magn Reson Med 1994;31:495–503.

22. Ehman RL, Felmlee JP. Adaptive technique for high-definition MR imaging of moving structures. Radiology 1989;173:255–263.

23. Bruder H, Fischer H, Reinfelder H-E, Schmitt F. Image reconstruction for echo planar imaging with nonequidistant k-space sampling. Magn Reson Med 1992;23:311–323.

24. Wong EC. Shim insensitive phase correction for EPI using a two echo reference scan. In: Proceedings of the 11th Annual Meeting of SMRM, Berlin, Germany, 1992. p 4514.

25. Jesmanowicz A, Wong EC, Hyde JS. Phase correction for EPI using internal reference lines. In: Proceedings of the 12th Annual Meeting of SMRM, New York, 1993. p 1239.

26. Hu X, Le TH. Artifact reduction in EPI with phase-encoded reference scan. Magn Reson Med 1996;36:166–171.

27. Zhao X, Bodurka J, Jesmanowicz A, Li S-J. B_0-fluctuation–induced temporal variation in EPI images series due to the disturbance of the steady-state free precession. Magn Reson Med 2000;44:758–765.

28. Lu H, Jesmanowicz A, Mazaheri Y, Hyde JS. Reference scan navigator-aided half k-space interleaved EPI for high resolution fMRI at 3 T. In: Proceedings of the 10th Annual Meeting of ISMRM, Honolulu, 2002. p 2372.

29. Nguyen TD, Wang Y, Watts R, Mitchell I. k-Space weighted least-squares algorithm for accurate and fast motion extraction from magnetic resonance navigator echoes. Magn Reson Med 2001;46:1037–1040.

30. Wong EC, Boskamp E, Hyde JS. A volume optimized quadrature elliptical endcap birdcage brain coil. In: Proceedings of the 11th Annual Meeting of SMRM, Berlin, Germany, 1992. p 4015.

31. Hyder F, Behar KL, Martin MA, Shulman RG. Dynamic magnetic resonance imaging of the rat brain during fore-paw stimulation. J Cereb Blood Flow Metab 1994;14:649–655.

32. Yang X, Hyder F, Shulman RG. Activation of single whisker barrel in rat brain localized by functional magnetic resonance imaging. Proc Natl Acad Sci USA 1996;93:475–478.

33. Lu H, Jesmanowicz A, Hyde JS. A technique for Hessian matrix formation for gradient coil optimization. In: Proceedings of the 10th Annual Meeting of ISMRM, Honolulu, 2002. p 813.

34. Gerrits RJ, Stein EA, Greene AS. Laser-Doppler flowmetry utilizing a thinner skull cranial window preparation and automated stimulation. Brain Res Brain Res Protoc 1998;3:14–21.

35. Paxino G, Watson C. The rat brain in stereotaxic coordinates. San Diego: Academic Press; 1998.

36. Mandeville JB, Marota JJA, Kosofsky BE, Keltner JR, Weissleder R, Rosen BR, Weisskoff RM. Dynamic functional imaging of relative cerebral blood volume during rat forepaw stimulation. Magn Reson Med 1998;39:615–624.

37. Ogawa S, Lee TM, Stepnoski R, Chen W, Zhu XH, Ugurbil K. An approach to probe some neural systems interaction by functional MRI at neural time scale down to milliseconds. Proc Natl Acad Sci USA 2000;97:11026–11031.

38. Cox RW, Hyde JS. Software tools for analysis and visualization of fMRI data. NMR Biomed 1997;10:171–178.

39. Bandettini PA, Jesmanowicz A, Wong EC, Hyde JS. Processing strategies for time-course data sets in functional MRI of the human brain. Magn Reson Med 1993;30:161–173.

40. Welker C, Woolsey TA. Structure of layer IV in the somatosensory neocortex of the rat: description and comparison with mouse. J Comp Neurol 1974;158:437–454.

41. Boxerman JL, Hamberg LM, Rosen BR, Weisskoff RM. MR contrast due to intravascular magnetic susceptibility perturbations. Magn Reson Med 1995;34:555–566.

42. Logothetis NK, Merkle H, Augath M, Trinath T, Ugurbil K. Ultra high-resolution fMRI in monkeys with implanted RF coils. Neuron 2002;35:227–242.

43. Harel N, Zhao F, Wang P, Kim S-G. Cortical layer specificity of BOLD and CBV fMRI signals at ultra-high resolution. In: Proceedings of the 10th Annual Meeting of ISMRM, Honolulu, 2002. p 9.